physica status solidi (a)

RESEARCH ARTICLE OPEN ACCESS

Scalable Growth and Properties of $(Al_xGa_{1-x})_2O_3$ Thin Films on 2- and 4-Inch Sapphire via Close-Coupled Showerhead MOCVD

Ciaran Paul Llewelyn[1] | Zdenko Zápražný[2] | Edmund Dobročka[2] | Filip Gucmann[2] | Dan Lamb[1]

[1]The Oxide and Chalcogenide Facility, Centre for Integrative Semiconductor Materials (CISM), Faculty of Science and Engineering, Bay Campus, Swansea University, Swansea, UK | [2]Institute of Electrical Engineering, Slovak Academy of Sciences, Bratislava, Slovakia

Correspondence: Dan Lamb (d.a.lamb@swansea.ac.uk)

Received: 23 July 2025 | **Revised:** 3 December 2025 | **Accepted:** 12 February 2026

Keywords: 4-inch sapphire | aluminium gallium oxide | gallium oxide | MOCVD | semiconductors

ABSTRACT

A series of $(Al_xGa_{1-x})_2O_3$ thin films were deposited using an AIXTRON Close-Coupled Showerhead (CCS) metalorganic chemical vapour deposition (MOCVD) system to study aluminium (Al) incorporation into the β-Ga_2O_3 lattice. Films ≈1.2 µm thick were grown on 2-inch and 4-inch c-plane sapphire substrates. A linear relationship between film composition and precursor ratio indicated near-ideal alloying behaviour. Growth kinetics were composition-dependent, where Al incorporation reduced growth rates compared to gallium (Ga), although pure Al_2O_3 grew faster than intermediate alloys. The films exhibited high optical transmittance (82–88%), with a tuneable bandgap increasing with Al content. Morphological changes and increased roughness were observed up to Al $x = 0.42$, suggesting a possible phase transition. X-ray diffraction, rocking curve measurements and pole figure confirmed the monoclinic β-phase for the Ga_2O_3 only film, with strong, well-defined Bragg peaks. For Al_2O_3, only the substrate and nucleation layer reflections were visible, consistent with epitaxial Al_2O_3 growth on sapphire. The largest rocking curve full width half maximum was observed for samples with Al content x equals 0.12 and 0.42, which can be correlated with significant changes in the thin film surface morphology. The successful extension from 2-inch to 4-inch wafers highlights the scalability and uniformity of the CCS MOCVD process.

1 | Introduction

The compound semiconductor $(Al_xGa_{1-x})_2O_3$ has gathered significant attention due to its tuneable ultra-wide bandgap (UWBG), which ranges from 4.9 eV ($x = 0$) to 8.8 eV ($x = 1$) [1]. This tunability makes it a promising material for applications in power electronics, deep-ultraviolet (UV) optoelectronics and high-frequency devices [2–8]. $(Al_xGa_{1-x})_2O_3$ can also serve as a barrier or spacer layer in heterostructure field-effect transistors (HFETs) and can therefore enable the formation of a 2D electron gas [2, 9]. The ability to adjust the bandgap by varying the Al content (x) allows for the optimisation of electronic and optical properties to meet specific device requirements. Bhuiyan et al. demonstrated the successful growth of $(Al_xGa_{1-x})_2O_3$ via metalorganic chemical vapour deposition (MOCVD) onto Fe-doped semi-insulating (010) β-Ga_2O_3 substrates [10]. Thin films with Al compositions of x up to 0.48 were deposited, having bandgaps ranging from 5.2 to >5.7 eV, highlighting potential use in advanced electronic applications.

The work by Zhang et al. demonstrated that the incorporation of an intermediate layer of $(Al_xGa_{1-x})_2O_3$ can mitigate the lattice mismatch-induced strain, facilitating the subsequent growth of high-quality β-Ga_2O_3 on sapphire substrates [11]. In a comprehensive study by Bhuiyan et al., $(Al_xGa_{1-x})_2O_3$ films were deposited on various orientations of semi-insulating β-Ga_2O_3 wafers via MOCVD [12]. Demonstrating, for this homoepitaxial approach, Al incorporation of $x = 0.16$, 0.29 and 0.99 as determined by high-resolution X-ray diffraction (HRXRD). MOCVD film thicknesses varied across all samples from 20 nm to 422 nm. Okumura et al. also reported MOCVD growth of $(AlGa)_2O_3$,

but in this case, pursuing α-phase by use of *m*-plane sapphire substrates [13]. Their growth conditions differed significantly from those used in the present work, employing triethylgallium with an argon carrier gas at temperatures ranging from 600°C to 950°C. The Al composition x, determined by HRXRD, was reported to be between 0 and 0.74. However, the absence of film thickness data makes their results difficult to compare directly with our study.

MOCVD is the preferred technique for the epitaxial growth of $(Al_xGa_{1-x})_2O_3$ due to its precise control over composition and uniformity. Studies of $(Al_xGa_{1-x})_2O_3$ commonly employ bulk β-Ga_2O_3 substrates to minimise lattice mismatch and reduce heterojunction stress [14]. In contrast, this study explores the use of significantly more cost-effective sapphire substrates to investigate the structural and optical properties of films across the full range of Al compositions.

The system used for this study was the AIXTRON Close-Coupled Showerhead (CCS) MOCVD, compatible with both 2-inch and 4-inch substrates. The CCS reactor design is particularly advantageous for this process, as it ensures a uniform distribution of precursor gases across the substrate surface, leading to high-quality film growth. A notable feature of the CCS reactor is the adjustable gap height. This is defined as the distance between the substrate on the graphite susceptor and the showerhead precursor inlet. This distance can be varied between 5 mm and 25 mm, enabling systematic investigation of precursor path length and boundary layer effects on the epitaxial films grown.

Several studies, above and beyond those already detailed, have reported the successful growth of $(Al_xGa_{1-x})_2O_3$ films via MOCVD [12–15]. However, to the best of the authors' knowledge, the research presented here is the first to transition from Ga_2O_3 through to Al_2O_3 thin films on both 2-inch and 4-inch sapphire substrates. In this work, a solitary x refers to the fraction of Al within the $(Al_xGa_{1-x})_2O_3$ film, taking a value of 0–1. The Al precursor molar flow ratio, Al/(Al+Ga), during growth is referred to as $x_{(Set)}$, while the measured film composition (from EDX) is denoted $x_{(Meas)}$.

A series of $(Al_xGa_{1-x})_2O_3$ thin films were grown to investigate the incorporation of Al into the β-Ga_2O_3 lattice. To eliminate thickness-related artefacts in the analysis, a target film thickness of 1.2 µm was maintained across all samples. The full series of $(Al_xGa_{1-x})_2O_3$ thin films were deposited on 2-inch c-plane sapphire (0001) substrates. Additionally, the 4-inch growth capability was demonstrated by depositing on c-plane sapphire wafers with an 8.0° miscut towards the (10–10) plane. For the $(Al_xGa_{1-x})_2O_3$ thin films deposited on 4-inch sapphire wafers, an $x_{(Set)}$ precursor molar flow ratios of 0, 0.5 and 1.0 were used to assess thickness uniformity and continuity of film properties in comparison to the 2-inch samples.

2 | Experimental

A series of $(Al_xGa_{1-x})_2O_3$ thin films were deposited using an AIXTRON CCS reactor on 2-inch sapphire c-plane (0001) substrates and 4-inch sapphire c-plane (0001) substrates with an 8.0° miscut towards (10–10). Both substrates were 430 µm thick and double-side polished. Trimethylgallium (TMGa) and trimethylaluminium (TMAl) were used as the Ga and Al precursors, respectively, while 5N oxygen (O_2) was used as the oxidant. High-purity nitrogen gas was employed as the carrier gas, whilst growth temperatures of 925°C and 950°C were used for the $(Al_xGa_{1-x})_2O_3$ thin films on 2-inch and 4-inch wafers, respectively.

The flow rates for the Ga and Al precursors ranged from 13 µmol/min to 68 µmol/min, with an O_2 flow rate of 4.4×10^4 µmol/min. The growth temperature for all 2-inch samples was maintained at 925°C. Prior to the growth step, the sapphire substrates were annealed at 720°C for 10 min under an ambient flow of O_2. This was followed by the deposition of a ≈30 nm nucleation layer of Ga_2O_3 at 650°C, exhibiting β-Ga_2O_3 crystallographic characteristics. This was to ensure preferential growth and improved crystalline quality of the subsequent thin films [16].

The $(Al_xGa_{1-x})_2O_3$ layer, with x varying from 0 to 1, targeted a film thickness of 1.2 µm for each growth run. The chamber pressure, for the main growth, was maintained at 50 mbar with a total flow of 9 standard litres per minute, with susceptor rotation set to 60 rpm. The growth rate was monitored using a LayTec EpiTT system, which provided real-time reflectance monitoring at 405 nm, 633 nm and 950 nm.

X-ray diffraction (XRD) measurements of $(Al_xGa_{1-x})_2O_3$ films deposited on 2-inch c-plane sapphire substrates via MOCVD were performed using a Panalytical X'pert^3 MRD diffractometer with a Cu anode operating at 1.8 kW (45 kV, 40 mA). Measurements were performed in a high-resolution parallel beam set-up with a parabolic Goebel mirror and four-crystal monochromator providing Cu Kα1 ($\lambda =$ 1.5406 Å) X-ray radiation. Diffraction patterns of the films were recorded over a 2θ range of 15°–80°, using a parallel-plate collimator in front of the detector with an equatorial acceptance angle of 0.18°. A step size was 0.01° and a scan time of 1 s per step. All measurements were conducted at room temperature.

Transmittance measurements were performed using a Cary 5000 spectrophotometer, scanning over the wavelength range of 200–1000 nm. To determine the direct-like optical bandgap for the series of films with varying $x_{(Meas)}$, the Tauc relation was applied.

Elemental composition analysis was carried out using a Hitachi TM3000 scanning electron microscope (SEM) equipped with an Oxford Instruments energy-dispersive X-ray spectroscopy (EDX) detector. Measurements were performed at an accelerating voltage of 15 keV to ensure sufficient excitation of characteristic X-rays for a broad range of elements. The working distance was maintained at 7 mm, which is optimal for EDX detection efficiency in this system.

PeakForce tapping mode atomic force microscopy (AFM) measurements were performed using a Bruker Dimension Icon XR System operated in ScanAsyst mode. A ScanAsyst-Air probe (Bruker) was used for all measurements. Scans were acquired with a scan size of 5 × 5 µm, a resolution of 512 samples per line and a scan rate of 0.5 Hz. The acquired scans were processed and analysed using the Gwyddion open-source software (V2.67).

3 | Results and Discussion

The AIXTRON CCS MOCVD reactor, shown in Figure 1, features a flexible susceptor configuration, accommodating either three 2-inch wafers or one 4-inch wafer on high-quality silicon carbide-coated graphite susceptors, optimised for uniform temperature distribution. The system allows precise control over rotation speed, enhancing film homogeneity, and includes an adjustable

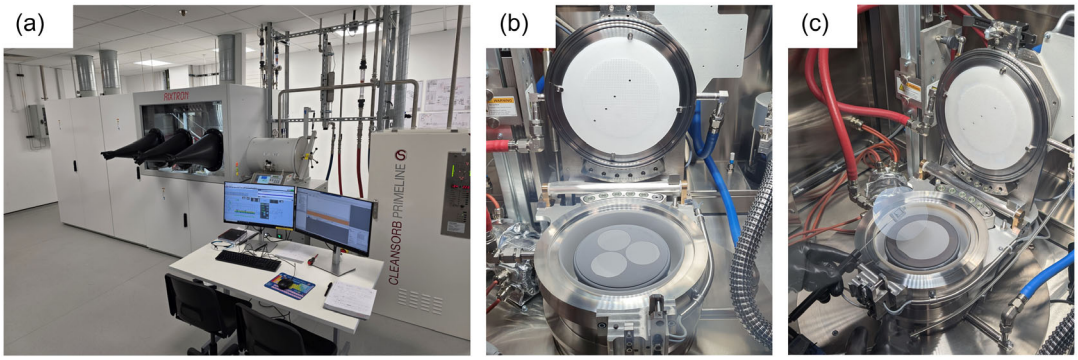

FIGURE 1 | (a) AIXTRON CCS MOCVD reactor designed for both oxide and chalcogenide thin film growth, located within Swansea University's state-of-the-art Centre for Integrative Semiconductor Materials building. (b) Open stainless steel CCS reaction chamber with quartz deposition shield and 3 × 2-inch pocket graphite susceptor. (c) Open chamber with 1 × 4-inch pocket graphite susceptor and 4-inch $(Al_xGa_{1-x})_2O_3$ coated sapphire wafer being removed with vacuum tweezers.

susceptor-to-showerhead gap height ranging from 5 mm to 25 mm, enabling the optimisation of precursor flow dynamics, gas-phase reactions, and growth uniformity [16]. The growth rate of the $(Al_xGa_{1-x})_2O_3$ thin films was calculated using a 633 nm laser reflectance from the LayTec EpiTT, utilising the bespoke EpiTT software.

To determine the optimum growth conditions for the $(Al_xGa_{1-x})_2O_3$ thin film series, a brief preliminary study on the factors influencing the β-Ga_2O_3 growth rate was conducted, where the impact of various growth parameters on the deposition rate was investigated (Figure 2). First, a baseline β-Ga_2O_3 growth recipe was employed with a TMGa molar flow rate of 42.4 µmol/min at 930°C under a reactor pressure of 50 mbar, with the adjustable gap height set to 9 mm, yielding a growth rate of 0.88 µm/h.

The second growth in this study focused specifically on the influence of the adjustable gap height. The gap height was reduced from 9 mm to 6 mm for the second growth, and this resulted in a 39% increase, with a growth rate of 1.23 µm/h. This improvement can be attributed to the shorter diffusion path for precursor molecules, which enhances transport efficiency to the substrate. Additionally, the higher precursor concentration near the substrate interface promotes material incorporation and increases precursor utilisation.

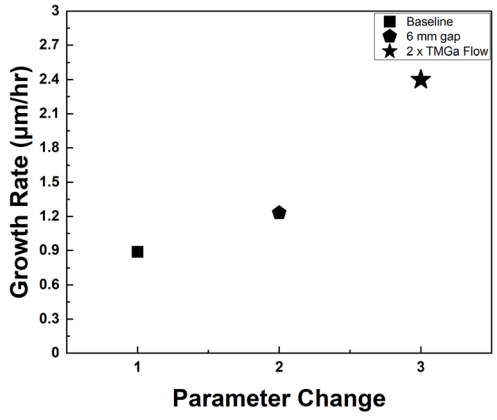

FIGURE 2 | Growth rate (µm/h) versus growth parameter change. (1) Square—Baseline recipe, TMGa Flow = 42.4 µmol/min with a 9 mm gap. (2) Pentagon—TMGa Flow = 42.4 µmol/min with a 6 mm gap, (3) Star—TMGa Flow = 85 µmol/min with a 6 mm gap.

The final optimisation variable in this study looked at how an increase in the flow rate of TMGa precursor influenced the growth rate. The flow rate of the TMGa was doubled from 42.4 µmol/min to 85 µmol/min, while maintaining the reduced gap height of 6 mm from the previous growth run. The growth rate increased by ~95% from 1.23 µm/h to 2.4 µm/h. This dramatic increase in growth rate can be attributed to the higher TMGa concentration, as the O_2 remains in significant excess and does not limit the β-Ga_2O_3 growth kinetics. Reported growth rates in the literature typically range between 1 and 3 µm/h, with the highest reported rate reaching 10 µm/h [17].

This growth rate study showcased the significant enhancement of film deposition rate from reducing the gap height and increasing the molar flow of TMGa. For clarity, throughout this study, the precursor molar flow ratio used during growth is written as $x_{(Set)}$, calculated as [TMAl]/([TMAl] + [TMGa]), while $x_{(Meas)}$ represents the Al fraction determined by EDX, calculated as Al at.%/(Al + Ga). Table 1 details the series of varying Al composition $x_{(Set)}$ growth runs, using the 6 mm gap height and a slightly reduced maximum ~68 µmol/min flow for the TMGa + TMAl.

For the growth series focused on the 2-inch substrates, the TMGa flow rate was gradually reduced for each run, as can be seen in Table 1. Conversely, the TMAl flow rate was increased for each run until Al_2O_3 was formed. This control was implemented to ensure a consistent total metalorganic precursor flow was used for the growth series, with a combined metalorganic flow rate of 68.3 µmol/min for TMGa and TMAl. For the secondary study, which focused on the 4-inch wafers, three growth runs were conducted. $x_{(Set)}$ was investigated at nominal values of 0, 0.489 and 1.0 for the respective growth runs. A fixed O_2 flow rate (4.4×10^4 µmol/min) was used for each growth run, with the O_2 in significant excess of the stoichiometric requirements to ensure that the process is metal-limited. Growth temperatures of 925°C and 950°C were used for the $(Al_xGa_{1-x})_2O_3$ thin films on 2-inch and 4-inch wafers, respectively. Film thicknesses for all samples in this study remain consistent between 1200 and 1230 nm, demonstrating the high level of precision of the CCS MOCVD, despite the changes in the precursors from $x_{(Set)} = 0$–1. The same trends are observed for the secondary study focusing on 4-inch wafers; however, a marginal increase in growth rate is observed relative to the analogous 2-inch study due to the higher growth temperature.

TABLE 1 | Growth data for series of $(Al_xGa_{1-x})_2O_3$ thin films varying $x_{(Set)}$ from 0 to 1.

Thin Film	Substrate size	TMGa flow, µmol/min	TMAl flow, µmol/min	$x_{(Set)}$ = [TMAl]/([TMAl] + [TMGa])	*d*, nm	Growth rate, µm/h
β-Ga_2O_3	2″	68.3	0	0	1202	1.79
$(Al_xGa_{1-x})_2O_3$	2″	58.1	11.6	0.167	1221	1.62
$(Al_xGa_{1-x})_2O_3$	2″	44.6	22.6	0.336	1225	1.45
$(Al_xGa_{1-x})_2O_3$	2″	35.7	34.2	0.489	1228	1.46
$(Al_xGa_{1-x})_2O_3$	2″	22.3	45.1	0.669	1230	1.35
$(Al_xGa_{1-x})_2O_3$	2″	13.4	56.7	0.809	1222	1.36
Al_2O_3	2″	0	68.3	1	1232	1.6
Ga_2O_3	4″	68.3	0	0	1236	1.87
$(Al_xGa_{1-x})_2O_3$	4″	35.7	34.2	0.489	1218	1.44
Al_2O_3	4″	0	68.3	1	1220	1.93

Table 2 summarises the optical and structural properties of the $(Al_xGa_{1-x})_2O_3$ films grown on 2-inch sapphire substrates. It shows the relationship between the precursor ratio $x_{(Set)}$, the alloy composition measured by EDX $x_{(Meas)}$, optical bandgap (eV) and surface roughness (AFM rms) and the XRD angle 2θ (°) and full width half maximum (FWHM) (°).

3.1 | EDX

The EDX measurements $x_{(Meas)}$ show that the Al content increases with increasing precursor ratio $x_{(Set)}$, as shown in Figure 3. A linear relationship is observed between $x_{(Meas)}$ and $x_{(Set)}$. This plot represents the relationship between the solid-phase composition of the alloy and the vapour-phase precursor flow ratio. The observed linear relationship highlights the near-ideal behaviour of the alloy system. This suggests minimal compositional deviation during growth, as evidenced by a segregation coefficient approaching unity (1.02), indicating uniform incorporation of species into the growing crystal. The small negative intercept (0.05) suggests the system might slightly under-incorporate at low precursor ratios, but the overall linearity supports a very well-behaved alloy system. The data highlight the CCS tools' level of control of alloy composition tuning in $(Al_xGa_{1-x})_2O_3$ films via precursor ratio adjustments.

The relationship between $x_{(Meas)}$ and growth rate is depicted in Figure 4. The growth of $(Al_xGa_{1-x})_2O_3$ showcases a clear decrease

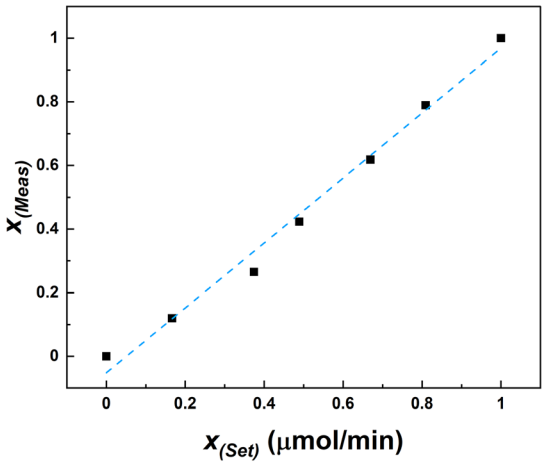

FIGURE 3 | Variation of $x_{(Meas)}$ as a function of $x_{(Set)}$ showing a linear correlation.

in growth rate as $x_{(Meas)}$ increases. This highlights the lower reactivity and potential competing surface reactions between TMAl and TMGa metalorganic precursors. The reduced surface mobility of the Al species, which can be attributed to the stronger Al–C bond, limits the overall growth kinetics, leading to slower growth rates as a function of $x_{(Meas)}$. Despite this limitation, the growth rate range is relatively narrow, between 1.36 and 1.62 µm/h, and as $x_{(Meas)}$ increases beyond 0.5–0.8, the rate at which the growth

TABLE 2 | Optical and structural properties of $(Al_xGa_{1-x})_2O_3$ thin films on 2-inch sapphire wafers.

Thin film	$x_{(Set)}$, µmol/min	$x_{(Meas)}$ Al at.%/(Al + Ga)	Bandgap, eV	rms, nm	$(\bar{2}01)2\theta$, °	XRC FWHM, °
β-Ga_2O_3	0	0	4.9	6.8	18.904	1.384
$(Al_xGa_{1-x})_2O_3$	0.167	0.12 ± 0.05	5.15	5.3	18.972	1.631
$(Al_xGa_{1-x})_2O_3$	0.336	0.27 ± 0.05	5.39	32.5	19.090	1.263
$(Al_xGa_{1-x})_2O_3$	0.489	0.42 ± 0.05	5.5	49.8	19.117	1.866
$(Al_xGa_{1-x})_2O_3$	0.669	0.62 ± 0.05	6	26.9	19.081	1.360
$(Al_xGa_{1-x})_2O_3$	0.809	0.80 ± 0.05	—	23.1	19.037	1.255
Al_2O_3	1	1	—	21.6	19.019	1.094

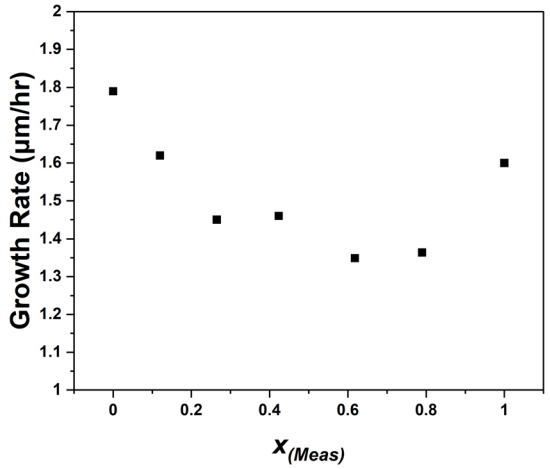

FIGURE 4 | Variation of growth rate (μm/h) as a function of $x_{(Meas)}$.

rate decreases begins to plateau. However, for the Al_2O_3 thin film (no TMGa precursor), the growth rate recovers from 1.36 to 1.6 μm/h. This recovery can be directly attributed to the full exclusion of TMGa from the reaction chamber, which removes the possibility of competing reactions at the substrate interface.

3.2 | Optical Transmittance

Figure 5 presents the optical transmittance (%) as a function of wavelength (nm) for the $(Al_xGa_{1-x})_2O_3$ series of thin films, referenced to air. Across all compositions, the films exhibit high transmittance (82–88%) in the visible and near-infrared regions. The inclusion of a bare sapphire substrate reveals that it contributes most of the transmittance losses over this wavelength range. The presence of interference fringes in the 300–1000 nm range indicates that the $(Al_xGa_{1-x})_2O_3$ films are optically smooth and uniform across most compositions. An exception is observed at $x_{(Meas)} = 0.42$, where the thin film is visibly cloudy and exhibits a relatively featureless transmittance spectrum, suggesting increased scattering and reduced optical quality. The higher transmittance observed for the $x_{(Meas)} = 0.8$ and $x_{(Meas)} = 1$ films compared to the bare substrate likely arises due to thin-film interference and anti-reflection effects. These films likely exhibit optimal optical thickness and smoothness, which minimise surface reflection and scattering, allowing more light to transmit through the structure than the uncoated sapphire substrate alone.

As $x_{(Meas)}$ increases, the absorption edge shifts to lower wavelengths (higher energies). For $x_{(Meas)} = 0$ (pure Ga_2O_3), the absorption edge is near ~260 nm. For $x_{(Meas)} = 1$ (pure Al_2O_3), the absorption edge is not fully captured due to the limitations of the Cary 5000 spectrometer (200–3300 nm). The shift in absorption edge suggests an increase in optical bandgap with higher Al incorporation, consistent with expectations for $(Al_xGa_{1-x})_2O_3$ alloys. The inset presents the Tauc plot of $(\alpha E)^2$ versus energy (eV) and allows an approximation of the direct-like optical bandgap. This tunability confirms that Al incorporation directly modifies the electronic structures and allows access to a material with a wider bandgap that could prove suitable for deep-UV and high-power electronics [8, 18].

3.3 | Optical Bandgap Evaluation

Figure 6 highlights the optical bandgap as a function of varying the composition of the $(Al_xGa_{1-x})_2O_3$ thin films, $x_{(Meas)}$. A clear increase in the optical bandgap is observed as the Al content increases, ranging from 4.9 eV to 6.0 eV as $x_{(Meas)}$ approaches 0.6. The progressive widening of the bandgap is consistent with expectations for Al alloying, as the Al substitutes for Ga within the lattice. The optical bandgap for $x_{(Meas)} > 0.6$ has not been estimated due to the physical limitations of the UV source of the spectrophotometer.

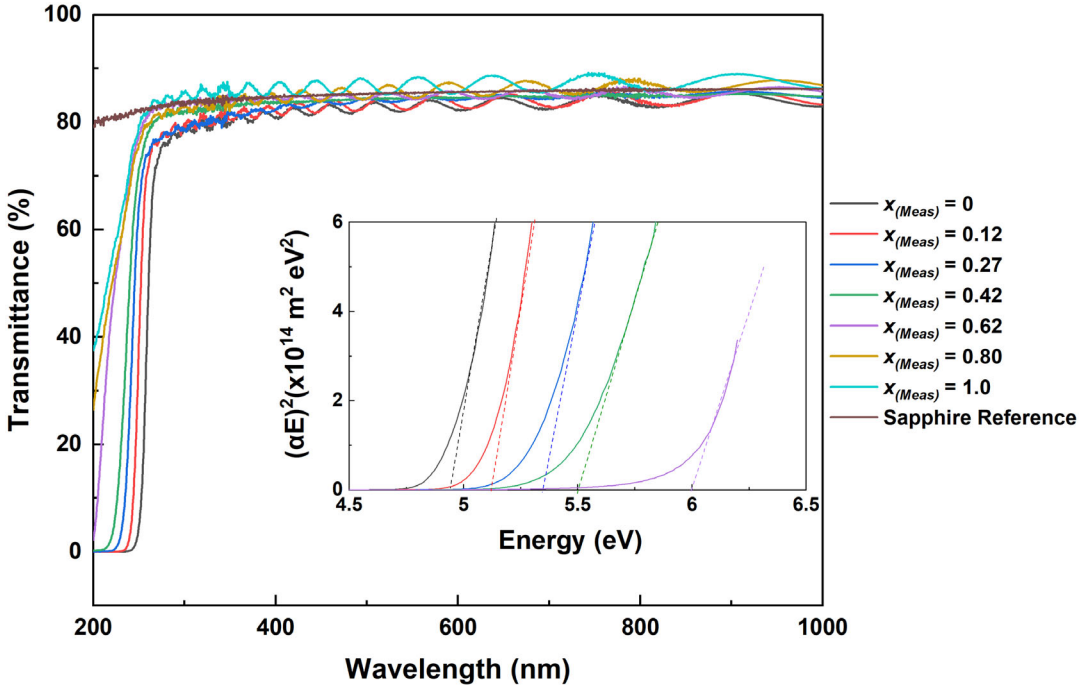

FIGURE 5 | Thin film transmittance (%) versus wavelength (nm). Inset is Tauc plot displaying $(\alpha E)^2$ versus energy (eV) for direct-like transitions.

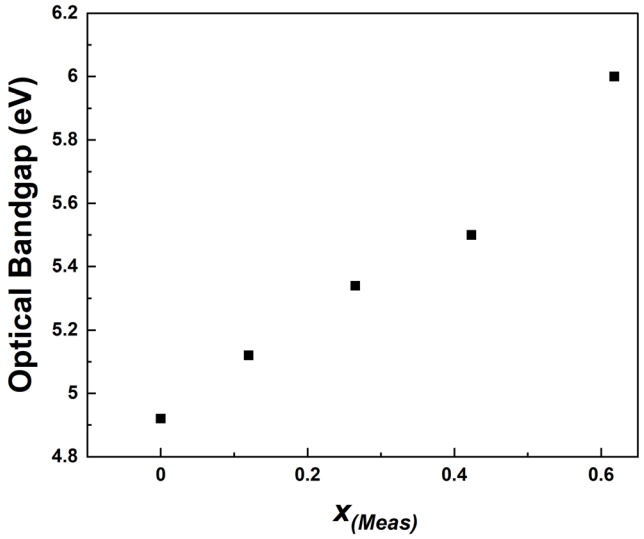

FIGURE 6 | Variation of optical bandgap (eV) as a function of composition $x_{(Meas)}$ determined by EDX.

3.4 | AFM

Figure 7 displays 5 μm × 5 μm AFM images of the thin films. An initial increase in Al from $x_{(Meas)}$ 0 to 0.12 leads to a marginal reduction in the mean surface roughness from 6.8 nm to 5.3 nm, with both exhibiting smooth and layered surfaces. However, the surface roughness increased significantly as the Al content rose from $x_{(Meas)}$ 0.12 up to 0.27 and 0.42 with rms values of 23.1 nm and 46.1 nm, respectively. This increase in surface roughness can be attributed to the presence of mixed phases as the Al content increases, which are a result of the competing β-$(Al_xGa_{1-x})_2O_3$ and γ-$(Al_xGa_{1-x})_2O_3$ phases. This phase change is seen within the AFM images as large, faceted grains. As the Al content further increases to $x_{(Meas)}$ 0.62, it is suggested that further transformation from the mixed phases to single γ-$(Al_xGa_{1-x})_2O_3$ results in smoother surfaces [10]. The rms continues to decrease as the Al content increases from $x_{(Meas)}$ 0.62 to 1, corresponding to a transition in morphology towards finer-grained structures. This growth series has displayed higher surface roughness values than seen within the literature for the growth of similar materials, with

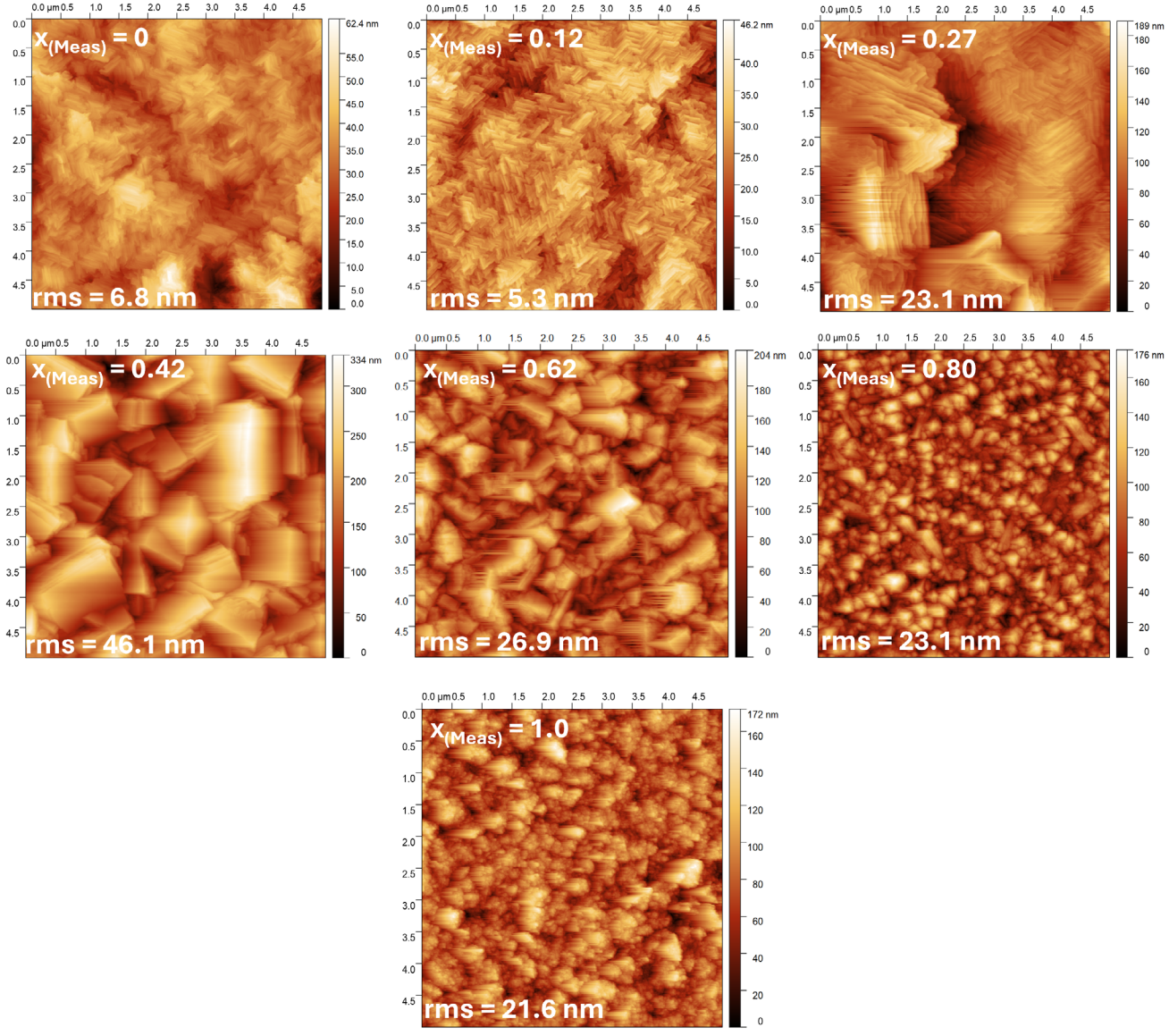

FIGURE 7 | AFM images (5 μm × 5 μm) of β-$(Al_xGa_{1-x})_2O_3$ thin films grown on c-plane sapphire substrates, with varying Al content from $x_{(Meas)} = 0$ to 1.

Bhuyian et al. highlighting surface roughness in the region of 1 nm–9 nm for their $(Al_xGa_{1-x})_2O_3$ thin films [12]. The higher surface roughness values illustrated in this work can be attributed to several key factors, including film thickness, where each film had a film thickness of 1200 nm, with thicker films naturally being rougher than their thinner counterparts. Additionally, this work demonstrates the heteroepitaxial growth of $(Al_xGa_{1-x})_2O_3$, which inherently exhibits greater lattice mismatch with the sapphire substrate compared with the homoepitaxial growth reported by Bhuyian et al.

3.5 | XRD

Figure 8 shows the high-resolution wide-angle symmetrical 2θ XRD patterns for 2-inch Ga_2O_3 ($x_{(Meas)} = 0$), $(Al_xGa_{1-x})_2O_3$ ($x_{(Meas)} =$ 0.12–0.8) and Al_2O_3 ($x_{(Meas)} = 1$) samples. Diffractograms reveal (0001) lattice plane reflections, related to the sapphire substrate and $\bar{2}01$, $\bar{4}01$ and $\bar{6}03$ diffractions, corresponding to the $(\bar{2}01)$ plane reflections of the β-Ga_2O_3 and β-$(Al_xGa_{1-x})_2O_3$ (found at ~18.9°, ~38.3° and ~59.0°, respectively for Ga_2O_3). Two weak signals located at ~31° and ~45° were attributed to the minor contribution of the (100)-oriented crystals with respective 400 and 600 diffractions. These reflections confirm the phase purity of the grown films. The presence of sharp, intense peaks indicates good crystallinity. No secondary phase peaks, such as those associated with α-Ga_2O_3 or amorphous contributions, are observed. At $x_{(Meas)} = 1$ (pure Al_2O_3), no new reflections are observed, suggesting that the Al_2O_3 thin film grows epitaxially on the c-plane sapphire substrate.

Figure 9 details the $\bar{2}01$ diffraction region from Figure 8, clearly showing the shift to the higher Bragg angles with increasing Al content. Higher Al content can lead to phase segregation in the monoclinic $(Al_xGa_{1-x})_2O_3$ alloy and co-existence of $(Al_xGa_{1-x})_2O_3$ crystallites with various Al content, which can affect the observed shift in the diffraction maxima [19, 20].

To confirm the epitaxial growth, the pole figure shown in Figure 10 was measured for the Ga_2O_3 sample ($x_{(Meas)} = 0$). 6 maxima corresponding to the 111 diffractions of the Ga_2O_3, and 3 maxima corresponding to the $10\bar{1}4$ diffractions of the sapphire substrate were observed. This confirms epitaxial growth of the

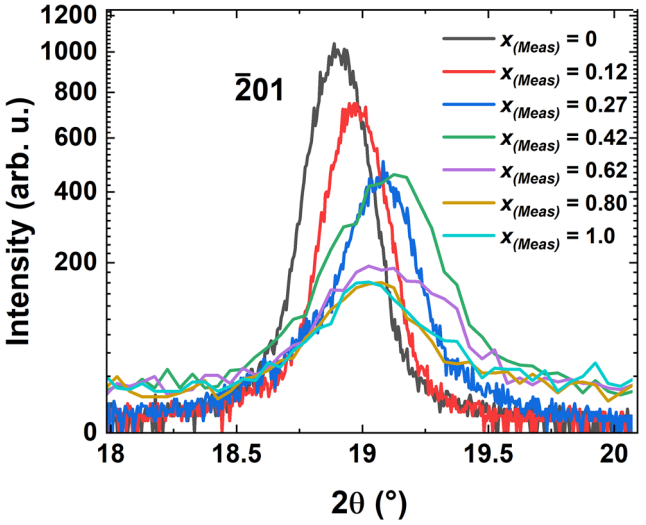

FIGURE 9 | Detail of $\bar{2}01$ diffraction maxima revealing the Bragg-angle shift with increasing Al content.

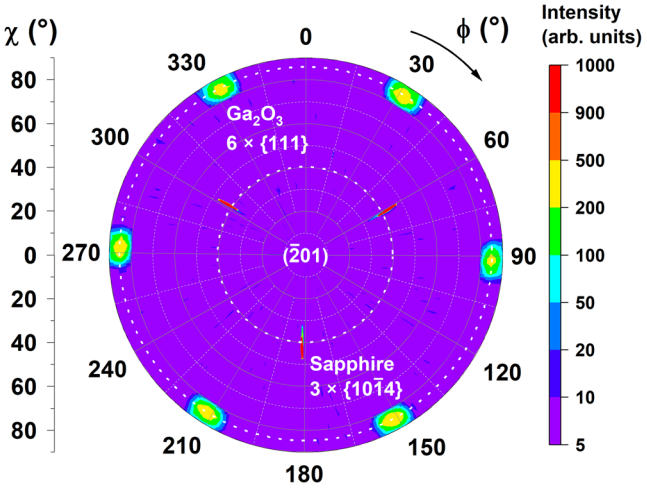

FIGURE 10 | Pole figure of Ga_2O_3 film confirming epitaxial growth of $(\bar{2}01)$ β-Ga_2O_3 on c-plane sapphire substrate.

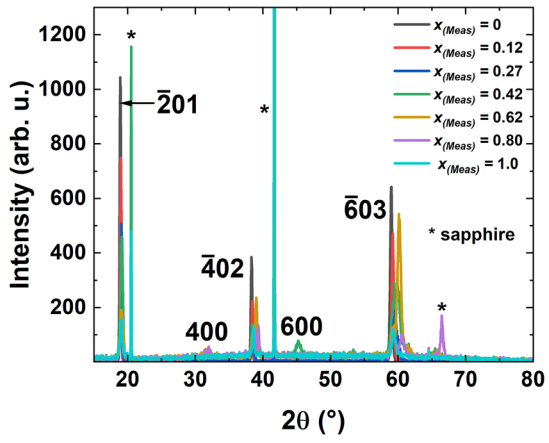

FIGURE 8 | High-resolution wide-angle symmetrical XRD scans of Ga_2O_3, $(Al_xGa_{1-x})_2O_3$ and Al_2O_3 samples.

Ga_2O_3 film on c-plane sapphire and the presence of 6 in-plane rotational domains observed in agreement with previous studies [15, 21, 22].

Figure 11 represents $\bar{2}01$ X-ray rocking curves (XRC) for all measured samples; FWHMs in the range of ~1.1°–1.9° were obtained, consistent with previous studies reporting MOCVD-grown Ga_2O_3 and $(Al_xGa_{1-x})_2O_3$ films on sapphire. Generally, higher XRC FWHMs can be ascribed to the enhanced films' mosaicity resulting from the presence of in-plane rotational domains, typically present in the $(\bar{2}01)$-oriented films grown on foreign substrates.

Figure 12 relates the XRC FWHM and the EDX-resolved Al content in the $Ga_2O_3/(Al_xGa_{1-x})_2O_3$ films. Largest FWHMs were observed for samples with $x_{(Meas)} = 0.12$ and 0.42, which can be correlated with significant changes in the film's surface morphology revealed by the AFM (Figure 7) and can suggest transitions between competing growth modes.

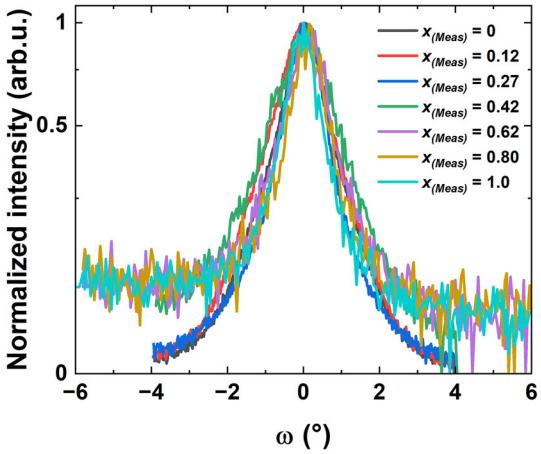

FIGURE 11 | $\bar{2}01$ X-ray rocking curves of Ga_2O_3, $(Al_xGa_{1-x})_2O_3$ and Al_2O_3 samples.

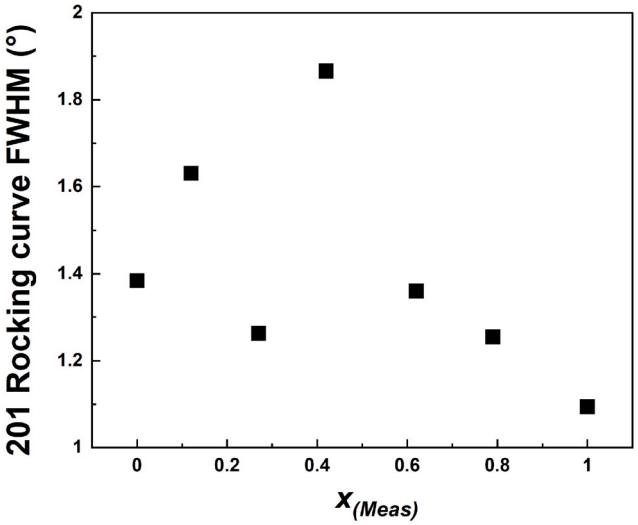

FIGURE 12 | $\bar{2}01$ X-ray rocking curve FWHM as a function of $x_{(Meas)}$.

3.6 | 2-Inch to 4-Inch Sapphire Wafer

In addition to the main investigation of the 2-inch samples discussed in this work, a small set of $(Al_xGa_{1-x})_2O_3$ thin films were grown on 4-inch wafers to assess the scalability of the CCS MOCVD process.

Table 3 summarises the characterisation data for the three 4-inch $(Al_xGa_{1-x})_2O_3$ samples grown on c-plane sapphire wafers with an 8° miscut towards the (10–10) direction, which was selected to promote step-flow growth. These data are presented to demonstrate the scalability of the CCS MOCVD tool from 2-inch to 4-inch substrates.

TABLE 3 | Morphological and optical data measured at the centre of $(Al_xGa_{1-x})_2O_3$ samples grown on c-plane sapphire wafers with an 8° miscut.

Bulk film	$x_{(Set)}$, µmol/min	$x_{(Meas)}$ Al at.%/(Al + Ga)	Bandgap, eV	rms, nm
β-Ga_2O_3	0	0	5.05	26.2
$(Al_xGa_{1-x})_2O_3$	0.489	0.41 ± 0.05	5.4	44.0
Al_2O_3	1	1.0	—	18.2

AFM roughness, EDX composition and optical bandgap were evaluated at the five cardinal positions on each wafer. The results indicate that the composition can be controlled reproducibly at the 4-inch scale, with the optical bandgap value following the expected trend with Al incorporation, increasing from 5.05 eV to 5.4 eV as $x_{(Meas)}$ increased from 0 to 0.41. The surface morphology, measured via AFM, follows a similar trend to that of the 2-inch analogues with increasing surface roughness as a result of the competing β-$(Al_xGa_{1-x})_2O_3$ and γ-$(Al_xGa_{1-x})_2O_3$ phases. There are significant discrepancies between the 2-inch and 4-inch Ga_2O_3 and Al_2O_3 thin-film analogues, which may be attributed to the 8° miscut. Investigating this effect will be the subject of a future publication.

4 | Conclusion

The systematic investigation of $(Al_xGa_{1-x})_2O_3$ thin films grown via Swansea University's AIXTRON CCS MOCVD on c-plane sapphire has demonstrated the capability to precisely control Al incorporation, structural quality and optical properties. The optimised growth conditions, including a reduced gap height and controlled precursor flow, enabled the deposition of high-quality films with smooth surfaces and uniform thicknesses. EDX analysis validated the efficient incorporation of Al into the lattice, allowing for the calculation of a segregation coefficient close to 1. This suggests the efficient incorporation of Al from the gas phase into the solid phase. The observed reduction in growth rate with increasing Al content, attributed to differences in precursor decomposition kinetics and surface diffusion, highlights the importance of precursor selection and growth parameter optimisation in achieving desired film properties. Transmittance measurements demonstrated a high average visible transparency and the tunability of the optical bandgap with increasing Al content, shifting from 4.9 eV for pure β-Ga_2O_3 to beyond 6.0 eV for Al-rich compositions. AFM showed that as Al content increased, smooth Ga-rich films evolved into rough, faceted grains at $x_{(Meas)}$ 0.4, then transitioned to fine-grained structures with moderate roughness at higher Al levels. XRD analysis confirmed the epitaxial growth, on the sapphire substrate, of both Ga_2O_3 and Al_2O_3. Overall, the higher XRC FWHMs (FWHMs ranging between 1.1° and 1.9°) observed in this study can be attributed to increased film mosaicity arising from in-plane rotational domains, which are characteristic of the $(\bar{2}01)$-oriented films grown on foreign substrates.

Overall, this study establishes a comprehensive understanding of the growth dynamics and material properties of $(Al_xGa_{1-x})_2O_3$ films deposited using CCS MOCVD. The ability to engineer bandgap, structural phases and surface morphology through precise growth control makes $(Al_xGa_{1-x})_2O_3$ a promising material for next-generation power electronics, deep-UV photodetectors and 2D electron gas structures. The successful transfer of the process from 2- to 4-inch wafer sizes highlights the scalability and uniformity capabilities of the CCS MOCVD system, demonstrating its suitability for larger-scale production and advanced device fabrication. Future work will focus on refining growth conditions to further enhance crystal quality, exploring doping strategies for

electrical conductivity modulation and integrating these films into device structures to assess their functional performance.

Acknowledgements

The authors sincerely thank Dr. Colin Paillet and Dr. Indraneel Sanyal of AIXTRON for their support in commissioning the Ga_2O_3 thin film growths on the CCS reactor. They also acknowledge the Engineering and Physical Sciences Research Council (EPSRC) for the Strategic Equipment funding (EP/T019085/1), which enabled the procurement of the MOCVD equipment and the development of thin film growth protocols. We acknowledge the funding from the Slovak Research and Development Agency (APVV-24-0325, SK-TW-RD-24-0006). The support from the team at the Centre for Integrative Semiconductor Materials (CISM) and Swansea University is gratefully acknowledged for their invaluable assistance in establishing the new MOCVD laboratory.

Funding

This study was supported by Engineering and Physical Sciences Research Council (EP/T019085/1); Agentúra na Podporu Výskumu a Vývoja (APVV-24-0325, SK-TW-RD-24-0006).

Data Availability Statement

The data that support the findings of this study are available from the corresponding author upon reasonable request.

References

1. H. Li, Z. Wu, S. Wu, P. Tian, and Z. Fang, "$(Al_xGa_{1-x})_2O_3$-Based Materials: Growth, Properties, and Device Applications," *Journal of Alloys and Compounds* 960 (2023): 170671, https://doi.org/10.1016/j.jallcom.2023.170671.

2. Y. Zhang, A. Neal, Z. Xia, et al., "Demonstration of High Mobility and Quantum Transport in Modulation-Doped β-$(Al_xGa_{1-x})_2O_3/Ga_2O_3$ Heterostructures," *Applied Physics Letters* 112 (2018): 173502, https://doi.org/10.1063/1.5025704.

3. Q. Feng, X. Li, G. Han, et al., "$(AlGa)_2O_3$ Solar-Blind Photodetectors on Sapphire With Wider Bandgap and Improved Responsivity," *Optical Materials Express* 7 (2017): 1240–1248, https://doi.org/10.1364/OME.7.001240.

4. F. F. Florena, A. Traoré, H. Okumura, R. Morita, Y. Jia, and T. Sakurai, "Investigation of Interface Traps in β-$(AlGa)_2O_3/Ga_2O_3$ Heterostructures by Dynamic Capacitance Dispersion Technique," *Applied Physics Letters* 125 (2024): 093503, https://doi.org/10.1063/5.0208449.

5. F. Liu, Y. Li, H. Cheng, C. Jin, and C. Liu, "Structural, Optical, and Electronic Properties of Epitaxial β-$(Al_xGa_{1-x})_2O_3$ Films for Optoelectronic Devices," *Advanced Optical Materials* 12 (2024): 2400724, https://doi.org/10.1002/adom.202400724.

6. A. Moore, S. Rafique, C. Llewelyn, D. Lamb, and L. Li, "A Review of Ga_2O_3 Heterojunctions for Deep-UV Photodetection: Current Progress, Methodologies, and Challenges," *Advanced Electronic Materials* 11 (2025): 2400898, https://doi.org/10.1002/aelm.202400898.

7. D. Herath Mudiyanselage, B. Da, J. Adivarahan, et al., "β-Ga_2O_3-Based Heterostructures and Heterojunctions for Power Electronics: A Review of the Recent Advances," *Electronics* 13 (2024): 1234, https://doi.org/10.3390/electronics13071234.

8. X. Xu, Z. Sheng, J. Shi, et al., "Tuning the Bandgaps of $(Al_xGa_{1-x})_2O_3$ Alloyed Thin Films for High-Performance Solar-Blind Ultraviolet Fully Covered Photodetectors," *Advanced Electronic Materials* 11 (2023): 2300042, https://doi.org/10.1002/adom.202300042.

9. S.-T. Chung, C. Langpoklakpam, Y. Dong, et al., "Effect of the AlGaO Spacer Layer on the Performance of β-Gallium Oxide Metal–Oxide Semiconductor Field Effect Transistors," *Advanced Electronic Materials* 11 (2025): e00291, https://doi.org/10.1002/aelm.v11.15.

10. A. F. M. A. U. Bhuiyan, Z. Feng, J. M. Johnson, et al., "Phase Transformation in MOCVD Growth of $(Al_xGa_{1-x})_2O_3$ Thin Films," *APL Materials* 8 (2020): 031104, https://doi.org/10.1063/1.5140345.

11. W. Zhang, H. Zhang, S. Zhang, et al., "The Heteroepitaxy of Thick β-Ga_2O_3 Film on Sapphire Substrate With a β-$(Al_xGa_{1-x})_2O_3$ Intermediate Buffer Layer," *Materials* 16 (2023): 2775, https://doi.org/10.3390/ma16072775.

12. A. F. M. A. U. Bhuiyan, L. Meng, H.-L. Huang, C. Chae, J. Hwang, and H. Zhao, "Al Incorporation up to 99% in Metalorganic Chemical Vapor Deposition-Grown Monoclinic $(Al_xGa_{1-x})_2O_3$ Films Using Trimethylgallium," *Phys. Status Solidi RRL – Rapid Research Letters* 17 (2023): 2300224, https://doi.org/10.1002/pssr.202300224.

13. H. Okumura and J. B. Varley, "MOCVD Growth of Si-Doped α-(AlGa) on m-Plane α-Substrates," *Japanese Journal of Applied Physics* 63 (2024): 075502, https://doi.org/10.35848/1347-4065/ad5cb2.

14. Y. Wang, L. Wang, Y. Dong, et al., "Compositional Engineering and Performance Optimization of β-(Al_xGa_{1-x}) via MOCVD Epitaxy," *Journal of Alloys and Compounds* 1031 (2025): 181060, https://doi.org/10.1016/j.jallcom.2025.181060.

15. M. U. Jewel, S. R. Crittenden, T. Hassan, et al., "Surface Properties of MOCVD Grown $(Al_{1-x}Ga_x)_2O_3$ Thin Films on c-Plane Sapphire via Scanning Kelvin Probe Microscopy," *AIP Advances* 14 (2024): 125029, https://doi.org/10.1063/5.0233458.

16. A. Waseem, G. M. Latham, C. McAleese, et al., "Comprehensive Study of β-Ga_2O_3 Epitaxial Growth Using a Variable Closed-Coupled Showerhead MOCVD Reactor," *Applied Physics Reviews* 12 (2025): 021412, https://doi.org/10.1063/5.0239454.

17. F. Alema, B. Hertog, A. Osinsky, P. Mukhopadhyay, M. Toporkov, and W. V. Schoenfeld, "Fast Growth Rate of Epitaxial β-Ga_2O_3 by Close Coupled Showerhead MOCVD," *Journal of Crystal Growth* 475 (2017): 77–82, https://doi.org/10.1016/j.jcrysgro.2017.06.001.

18. X. Ma, Y. Zhang, L. Dong, and R. Jia, "First-Principles Calculations of Electronic and Optical Properties of Aluminum-Doped β-Ga_2O_3 With Intrinsic Defects," *Results in Physics* 7 (2017): 1582–1589, https://doi.org/10.1016/j.rinp.2017.04.023.

19. A. F. M. Anhar Uddin Bhuiyan, Z. Feng, J. M. Johnson, et al., "MOCVD epitaxy of β-$(Al_xGa_{1-x})_2O_3$ Thin Films on (010) Ga_2O_3 Substrates and N-Type Doping," *Applied Physics Letters* 115 (2019): 120602, https://doi.org/10.1063/1.5123495.

20. H. W. Kim, H. Ko, Y.-C. Chung, and S. B. Cho, "Heterostructural Phase Diagram of Ga_2O_3-Based Solid Solution With Al_2O_3," *Journal of the European Ceramic Society* 41 (2021): 611–616, https://doi.org/10.1016/j.jeurceramsoc.2020.08.067.

21. H. Chouhan, E. Dobročka, P. Nádaždy, et al., "Rotational Domains and Origin of Improved Crystal Quality in Heteroepitaxial $(2\bar{2}01)$ β-Ga_2O_3 Films Grown on Vicinal Substrates by MOCVD," *Journal of Alloys and Compounds* 1044 (2025): 184481, https://doi.org/10.1016/j.jallcom.2025.184481.

22. G. Sfuncia, C. Bongiorno, G. Nicotra, et al., "Structural Insights into Nucleation and Grain Orientation in β-Ga_2O_3 Films Grown by MOVPE on Off-Axis 4H-SiC Substrates," *Applied Surface Science* 720 (2026): 165208, https://doi.org/10.1016/j.apsusc.2025.165208.